Simulation of Micro-/Macrosegregation during the Solidification of a Low-alloy Steel

Marc C. SCHNEIDER and Christoph BECKERMANN

Department of Mechanical Engineering, The University of Iowa, Iowa City, IA 52242, U.S.A.

A model for the solidification of multicomponent steels is presented and used to simulate the solidification of an austenitic steel. Assuming stationary solid phases, conservation of multiple species is considered simultaneously with the solution of the energy and Navier–Stokes equations, with full coupling of the temperature and concentrations through thermodynamic equilibrium requirements. By including finite-rate microscopic solid solute diffusion in the model, the solidus temperature of multicomponent austenitic steels can be accurately calculated. The extension of the model to incorporate a microscopic model of the peritectic transformation is described. A simulation of the austenitic solidification of a steel containing ten elements in a rectangular cavity cooled from the side shows the formation of macrosegregation, channel segregates, and islands of mush surrounded by the bulk melt. The global severity of macrosegregation of an element is found to be linearly dependent on its partition coefficient, although such scaling is not possible locally.

KEY WORDS: solidification; steel; peritectic transformation; thermosolutal convection; macrosegregation.

1. Introduction

In recent years, numerical simulations have shown the ability of macroscopic solidification models to predict the effects of convection in the mushy zone and bulk liquid on the development of an irregular liquidus front, flow channels in the mushy zone, local remelting of solid, and complicated macrosegregation and eutectic fraction distributions for the solidification of a variety of binary alloys.[1-8] Although this focus on binary systems has led to a greater understanding of the fundamental phenomena involved in alloy solidification, the solidification of commercially and technologically important multicomponent alloys (e.g., steels and nickel-base superalloys, respectively) involves an intricate coupling between buoyancy forces imparted by each element (as characterized by their differing solutal expansion coefficients) and microsegregation of each element (as characterized by their differing partition coefficients and solid mass diffusivities).[9]

Previous efforts at modeling macrosegregation in multicomponent steel alloys have suffered from the limitations of neglecting bulk liquid motion[10,11] or incomplete coupling of energy and species conservation in the mushy zone.[12-15] All of these models also assumed that microscopic diffusion of each element in the solid phase was either absent (Scheil type behavior) or complete (lever rule type behavior).

In a recent paper, the modeling of the formation of macrosegregation in steel due to multicomponent thermosolutal convection was explored in detail.[9] In the present study, that work is extended to include a microscopic model of the peritectic transformation. Results from a representative simulation of the solidification of a ten element austenitic steel in a rectangular cavity cooled from the side are also presented. Simulation results for the peritectic solidification of a multicomponent steel will be described in a separate study.

2. Model Description

The model is an extension of a model for binary alloy solidification[8,16,17] and can be obtained directly from the volume-averaged two-phase model of alloy solidification presented by Ni and Beckermann.[18] Since a detailed discussion of the macroscopic conservation equations is available elsewhere,[9] the focus here is on modeling of solid microsegregation and the peritectic transformation.

2.1. Macroscopic Conservation Equations

The macroscopic conservation equations in the model are summarized in **Table 1**. In deriving the equations, it has been assumed that there are at most three phases and three phase interfaces, i.e., ferrite (δ), austenite (γ) and liquid (ℓ) phases as well as δ/ℓ, γ/ℓ and γ/δ interfaces. Use has also been made of the fact that the interfacial areas (S) and phase change rates (Γ) at the k/j (or j/k) interface are related through $S_{kj} = S_{jk}$ and $\Gamma_{kj} = -\Gamma_{jk}$. In all of the equations, $\langle \Psi_k \rangle^k$ indicates the intrinsic volume average of a quantity Ψ of phase k, $\bar{\Psi}_{kj}$ indicates an average of a quantity Ψ of phase k over the k/j interfacial area in the averaging volume, and a superscript m indicates a value for solute m. The reader is referred to the Nomenclature for a complete description of all the symbols.

A number of assumptions have been made to arrive at the conservation equations in Table 1, including: stationary and rigid solid phases (i.e., no floating or settling of equiaxed crystals); thermal equilibrium and a solutally well mixed liquid within an averaging volume; negligible cross-diffusional effects between alloying elements; and the dissipative interfacial stress for flow through the mushy zone is modeled using an anisotropic permeability in analogy with Darcy's law. Since the cooling rates considered here are low, thermodynamic equilibrium is assumed to exist at the solid/ℓ and δ/γ interfaces so that the interfacial temperature and concentrations can be related through the simple phase equilibrium expressions shown in Table 1 (where the effects of each element on the liquidus ($T_{\ell s}$) and γ/δ-interface ($T_{\gamma\delta}$) temperatures are additive). Furthermore, in this study the changes in the liquidus and δ/γ-interface temperatures with concentration ($m_{\ell s}^m$ and

$m_{\gamma\delta}^m$) are assumed to be constant (but unequal) for each element, and the equilibrium partition coefficients ($\kappa_{\ell s}^m$ and $\kappa_{\gamma\delta}^m$) for each element are assumed to be constant. This simple approach to phase equilibrium cannot account for the formation of secondary phases or compounds due to strong interactions between the elements, and the authors anticipate incorporating more precise equilibrium calculations into the model in the future.

Since the focus of the following sections is on solid microsegregation, it is instructive to examine in detail the δ-solid species conservation equation in **Table 1** (with a similar analysis applicable to the γ-solid equation). This equation indicates that the rate of change of the volume average δ-solid concentration (left side) is balanced by the interfacial transfer of species at the δ/ℓ (first term on right) and δ/γ (second term on right) interfaces. The interfacial species transfer rate at the δ/j

Table 1. Summary of the governing equations for multicomponent peritectic solidification.

Mixture mass conservation

$$\frac{\partial}{\partial t}(\varepsilon_\ell \rho_\ell) + \nabla \cdot (\varepsilon_\ell \rho_\ell \langle v_\ell \rangle^\ell) = -\frac{\partial}{\partial t}(\varepsilon_\delta \rho_\delta) - \frac{\partial}{\partial t}(\varepsilon_\gamma \rho_\gamma)$$

Ferrite (δ) mass conservation

$$\frac{\partial}{\partial t}(\varepsilon_\delta \rho_\delta) = \Gamma_{\delta\ell} - \Gamma_{\gamma\delta}$$

Austenite (γ) mass conservation

$$\frac{\partial}{\partial t}(\varepsilon_\gamma \rho_\gamma) = \Gamma_{\gamma\ell} + \Gamma_{\gamma\delta}$$

Liquid species conservation

$$\varepsilon_\ell \rho_\ell \frac{\partial \langle C_\ell^m \rangle^\ell}{\partial t} + \varepsilon_\ell \rho_\ell \langle v_\ell \rangle^\ell \cdot \nabla \langle C_\ell^m \rangle^\ell = \nabla \cdot (\varepsilon_\ell \rho_\ell D_\ell^m \nabla \langle C_\ell^m \rangle^\ell)$$

$$+ [\langle C_\ell^m \rangle^\ell - \bar{C}_{\delta\ell}^m]\Gamma_{\delta\ell} + [\langle C_\ell^m \rangle^\ell - \bar{C}_{\gamma\ell}^m]\Gamma_{\gamma\ell} + S_{\delta\ell}\frac{\rho_\delta D_\delta^m}{l_{\delta\ell}^m}[\langle C_\delta^m \rangle^\delta - \bar{C}_{\delta\ell}^m] + S_{\gamma\ell}\frac{\rho_\gamma D_\gamma^m}{l_{\gamma\ell}^m}[\langle C_\gamma^m \rangle^\gamma - \bar{C}_{\gamma\ell}^m]$$

Ferrite (δ) species conservation

$$\varepsilon_\delta \rho_\delta \frac{\partial \langle C_\delta^m \rangle^\delta}{\partial t} = [\bar{C}_{\delta\ell}^m - \langle C_\delta^m \rangle^\delta]\left\{\Gamma_{\delta\ell} + S_{\delta\ell}\frac{\rho_\delta D_\delta^m}{l_{\delta\ell}^m}\right\} + [\bar{C}_{\delta\gamma}^m - \langle C_\delta^m \rangle^\delta]\left\{-\Gamma_{\gamma\delta} + S_{\gamma\delta}\frac{\rho_\delta D_\delta^m}{l_{\delta\gamma}^m}\right\}$$

Austenite (γ) species conservation

$$\varepsilon_\gamma \rho_\gamma \frac{\delta \langle C_\gamma^m \rangle^\gamma}{\partial t} = [\bar{C}_{\gamma\ell}^m - \langle C_\gamma^m \rangle^\gamma]\left\{\Gamma_{\gamma\ell} + S_{\gamma\ell}\frac{\rho_\gamma D_\gamma^m}{l_{\gamma\ell}^m}\right\} + [\bar{C}_{\gamma\delta}^m - \langle C_\gamma^m \rangle^\gamma]\left\{\Gamma_{\gamma\delta} + S_{\gamma\delta}\frac{\rho_\gamma D_\gamma^m}{l_{\gamma\delta}^m}\right\}$$

γ/δ Interfacial species balance

$$[\bar{C}_{\gamma\delta}^m - \bar{C}_{\delta\gamma}^m]\Gamma_{\gamma\delta} + S_{\gamma\delta}\frac{\rho_\gamma D_\gamma^m}{l_{\gamma\delta}^m}[\bar{C}_{\gamma\delta}^m - \langle C_\gamma^m \rangle^\gamma] + S_{\gamma\delta}\frac{\rho_\delta D_\delta^m}{l_{\delta\gamma}^m}[\bar{C}_{\delta\gamma}^m - \langle C_\delta^m \rangle^\delta] = 0$$

Mixture energy conservation

$$\left[\varepsilon_\ell \rho_\ell \frac{\partial \langle h_\ell \rangle^\ell}{\partial T} + \varepsilon_\delta \rho_\delta \frac{\partial \langle h_\delta \rangle^\delta}{\partial T} + \varepsilon_\gamma \rho_\gamma \frac{\partial \langle h_\gamma \rangle^\gamma}{\partial T}\right]\frac{\partial T}{\partial t} + \varepsilon_\ell \rho_\ell \frac{\partial \langle h_\ell \rangle^\ell}{\partial T}\langle v_\ell \rangle^\ell \cdot \nabla T = \nabla \cdot \{(\varepsilon_\ell k_\ell + \varepsilon_\delta k_\delta + \varepsilon_\gamma k_\gamma)\nabla T\}$$

$$+ [\langle h_\ell \rangle^\ell - \langle h_\delta \rangle^\delta]\Gamma_{\delta\ell} + [\langle h_\ell \rangle^\ell - \langle h_\gamma \rangle^\gamma]\Gamma_{\gamma\ell} + [\langle h_\delta \rangle^\delta - \langle h_\gamma \rangle^\gamma]\Gamma_{\gamma\delta}$$

Liquid momentum conservation

$$\varepsilon_\ell \rho_\ell \frac{\partial \langle v_\ell \rangle^\ell}{\partial t} + \varepsilon_\ell \rho_\ell \langle v_\ell \rangle^\ell \cdot \nabla \langle v_\ell \rangle^\ell = -\varepsilon_\ell \nabla \langle p_\ell \rangle^\ell + \nabla \cdot (\varepsilon_\ell \mu_\ell \nabla \langle v_\ell \rangle^\ell) + \nabla \cdot (\varepsilon_\ell \mu_\ell [\nabla \langle v_\ell \rangle^\ell]^t)$$

$$+ \nabla \cdot \{\mu_\ell[\langle v_\ell \rangle^\ell \nabla \varepsilon_\ell + \nabla \varepsilon_\ell \langle v_\ell \rangle^\ell]\} + \langle v_\ell \rangle^\ell\left[\frac{\partial}{\partial t}(\varepsilon_\delta \rho_\delta) + \frac{\partial}{\partial t}(\varepsilon_\gamma \rho_\gamma)\right] - \varepsilon_\ell^2 \mu_\ell \boldsymbol{K}^{(2)-1}\langle v_\ell \rangle^\ell + \varepsilon_\ell \sigma_\ell \boldsymbol{g}$$

Thermodynamic equilibrium relations

$$T_{\ell s} = T_f + \sum_m m_{\ell s}^m \langle C_\ell^m \rangle^\ell \quad \text{and} \quad \bar{C}_{s\ell}^m = \kappa_{\ell s}^m \langle C_\ell^m \rangle^\ell \quad \text{where} \quad s = \delta \text{ or } \gamma$$

$$T_{\gamma\delta} = T_p + \sum_m m_{\gamma\delta}^m \bar{C}_{\gamma\delta}^m \quad \text{and} \quad \bar{C}_{\gamma\delta}^m = \kappa_{\gamma\delta}^m \bar{C}_{\gamma\delta}^m$$
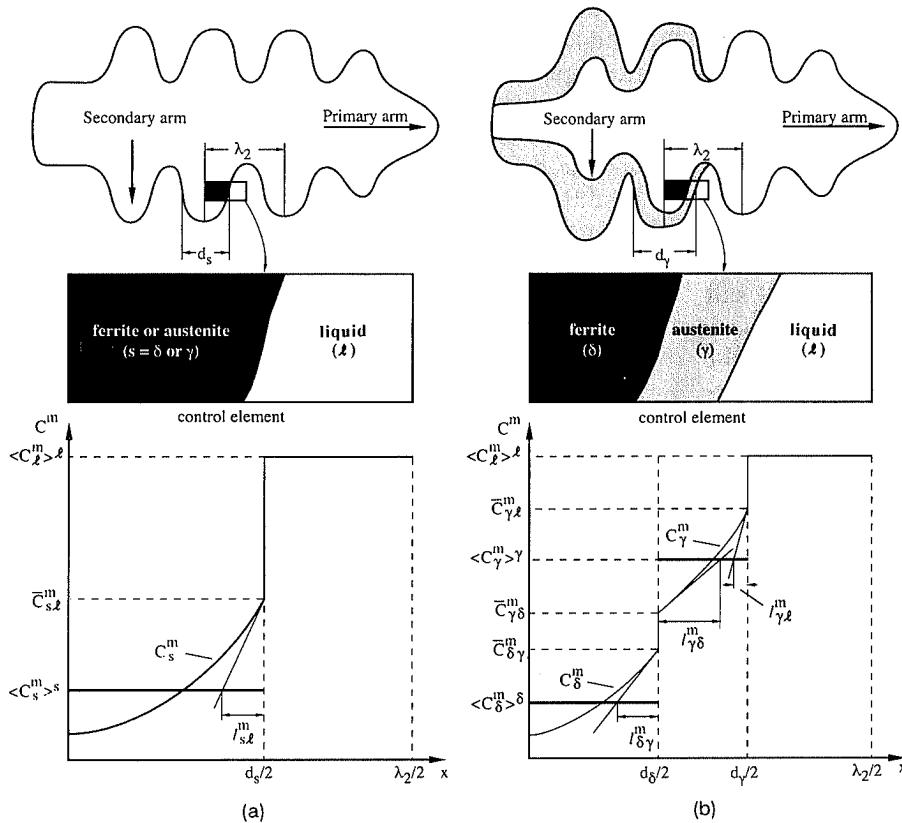
Fig. 1.
One-dimensional, plate-like model of a dendrite arm, illustration of the solid concentration profiles and illustration of the species diffusion lengths for: (a) primary (δ or γ) solidification and (b) peritectic solidification.

interface consists of two parts[19]: the first due to phase change and the second due to species diffusion in the solid at the interface. The interfacial species transfer rate due to diffusion is proportional to its driving force (the difference between the δ/j interfacial average and δ-solid volume average concentrations) as well as the δ/j interfacial area concentration, and inversely proportional to a solute diffusion length ($l_{\delta j}^m$) which characterizes the resistance to diffusion. Mathematically, a diffusion length is defined as

$$l_{kj}^m = [\bar{C}_{kj}^m - \langle C_k^m \rangle^k] \bigg/ \frac{\partial C_k^m}{\partial n}\bigg|_{kj} \quad \text{.....................(1)}$$

where the denominator represents the mean concentration gradient in phase k normal to the k/j interface.[19] The physical meaning of the various diffusion lengths that appear in Table 1 is illustrated in **Fig. 1**.

2.2. Solid Microsegregation

In modeling the solidification of steel there are three situations one must be concerned with: the formation of primary δ-solid above the peritectic temperature, the formation of primary γ-solid for alloys whose composition is greater than the peritectic, and peritectic solidification. **Figure 1(a)** illustrates the conditions on a microscopic scale for the first two cases (*i.e.*, δ- or γ-primary solidification) while **Fig. 1(b)** illustrates the microscopic conditions during peritectic solidification. During the peritectic transformation, γ-solid is assumed to form simultaneously from both the liquid and δ-solid, with the δ/γ transformation limited by solute diffusion through the γ-solid layer to the δ/γ interface.[20] This model of peritectic solidification has shown good agree-

ment between microsegregation predictions and measurements.[20-23]

The model used for the diffusion lengths was proposed by Wang and Beckermann[19] based on the work of Ohnaka[24] using the one-dimensional plate-like dendrite geometry shown in Fig. 1. A parabolic concentration distribution is assumed in the solid phases (both δ- and γ-solid) so that

$$C_s^m = a + bx + cx^2 \quad s = \delta \text{ or } \gamma \quad \text{.................(2)}$$

The determination of the coefficients in Eq. (2) is discussed in the following sections.

2.2.1. Diffusion Lengths for Primary Solidification

As shown in Fig. 1(a), for primary solidification only one of the solid phases (either δ- or γ-solid) is present, and the boundary conditions

$$\frac{dC_s^m}{dx} = 0 \text{ at } x = 0 \quad \text{and} \quad C_s^m = \bar{C}_{s\ell}^m \text{ at } x = d_s/2$$

$$s = \delta \text{ or } \gamma \quad \text{.........(3)}$$

can be applied to Eq. (2) along with the definition of the volume average concentration

$$\langle C_s^m \rangle^s = \frac{2}{d_s} \int_0^{d_s/2} C_s^m dx \quad s = \delta \text{ or } \gamma \quad \text{.............(4)}$$

Using Eqs. (2) through (4) the concentration profile in the solid can be determined which, in combination with Eq. (1), yields[19]

$$l_{s\ell}^m = d_s/6 \quad s = \delta \text{ or } \gamma \quad \text{......................(5)}$$

Based on the geometry in Fig. 1(a), the length d_s as well

as the interfacial area concentration $S_{s\ell}$ can, in turn, be related to the solid volume fraction and the secondary dendrite arm spacing as[19]

$$d_s = \varepsilon_s \lambda_2 \quad \text{and} \quad S_{s\ell} = 2/\lambda_2 \qquad s = \delta \text{ or } \gamma \quad \dots\dots\dots (6)$$

Note that substituting Eq. (6) into Eq. (5) yields a diffusion length that is equal for all species. However, since the rate of diffusion of an element in the solid on a microscopic scale also depends on its solid mass diffusivity, microsegregation for each element will still be different.

Using this approach, the solidus temperature for multicomponent alloys can be reproduced fairly accurately. Wang and Beckermann[25] have shown that,
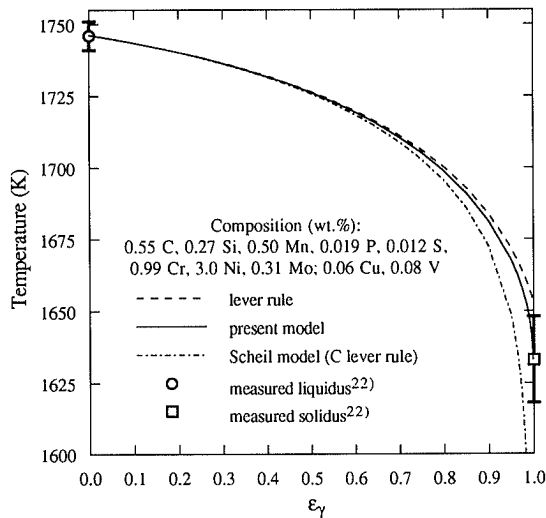
Fig. 2. Comparison of the evolution of the solid fraction with temperature for different solid microsegregation models. The lever rule was used to model carbon microsegregation for all cases, and the present model curve is for $\lambda_2 = 25 \mu m$, $t_f = 230$ sec and a parabolic solidification rate. Also shown are measured solidus and liquidus temperatures.[22]

Table 2. Initial concentrations, species dependent thermo-physical properties[10,21,30,31] and phase diagram parameters[33] ($T_f = 1\ 809$ K).

El.	C_{in}	$m_{\ell\gamma}^m$	$\kappa_{\ell\gamma}^m$	β_C^m	D_γ^m
C	0.8	−78	0.34	1.10×10^{-2}	5.6×10^{-10}
Si	0.15	−17.1	0.59	1.19×10^{-2}	5.6×10^{-13}
Mn	0.3	−3.32	0.75	1.92×10^{-3}	1.2×10^{-13}
S	0.01	−30.4	0.024	1.23×10^{-2}	3.3×10^{-11}
P	0.008	−27.1	0.09	1.15×10^{-2}	2.4×10^{-12}
Cu	0.2	−1.7	0.96	-5.48×10^{-4}	4.4×10^{-12}
Cr	0.1	−2.61	0.76	3.97×10^{-3}	1.2×10^{-12}
Ni	0.15	−1.6	0.94	-6.85×10^{-4}	1.9×10^{-13}
Mo	0.04	−3.25	0.56	-1.92×10^{-3}	1.8×10^{-13}

for no macroscopic transport of solute and a parabolic solidification rate, the solid and liquid species conservation equations in Table 1, together with Eqs. (4) and (6) and the thermodynamic equilibrium expressions from Table 1, provide an analytical relationship between the volume average liquid concentration of solute m, the solid fraction, and the partition coefficient and diffusion Fourier number ($\alpha^m = 4D_s^m t_f / \lambda_2^2$ where t_f is the local solidification time) for solute m. The $T-\varepsilon_\gamma$ curve shown in **Fig. 2** was generated using this analytical solution together with the liquidus temperature relation in Table 1, the properties in **Table 2**, $\lambda_2 = 25 \mu m$ and $t_f = 230$ s. (Note that the alloy in Fig. 2 is not the same as the one considered in the solidification simulations in Sec. 3.) The measured liquidus and solidus for the alloy, as well as $T-\varepsilon_\gamma$ curves where microsegregation is described by the lever rule or Scheil model, are also shown in Fig. 2. In addition, **Table 3** shows values of λ_2 that give solidus temperatures within the error associated with measuring the solidus for three austenitic steels, and they are reasonable for alloys of the given compositions.

During primary solidification, there is the possibility of local remelting of some of the solid that has formed. To avoid the difficulties associated with determining the local composition of the solid that is melting,[26,27] it is assumed that the average solid concentration of element m remains constant during remelting, i.e.,

$$\langle C_s^m \rangle^s = \text{constant during remelting} \quad s = \delta \text{ or } \gamma \quad \dots\dots (7)$$

2.2.2. Species Diffusion Lengths for Peritectic Solidification

The determination of the diffusion lengths for peritectic solidification follows that for primary solidification in Sec. 2.2.1. The microscopic geometry and dimensions are given in Fig. 1(b), and the parabolic concentration distribution given by Eq. (2) is assumed in both the δ- and γ-solids. The boundary conditions used to determine the coefficients for the solute distribution in the δ-solid are as given in Eq. (3) with $\overline{C}_{s\ell}^m$ and d_s replaced by $\overline{C}_{\delta\gamma}^m$ and d_δ, respectively. Following Eqs. (1) through (5), the diffusion length in the δ-solid at the δ/γ interface is then

$$l_{\delta\gamma}^m = d_\delta/6 \quad \dots\dots\dots\dots\dots\dots\dots (8)$$

Similarly, the length d_δ and the interfacial area concentration $S_{\delta\gamma}$ are readily shown to be

$$d_\delta = \varepsilon_\delta \lambda_2 \quad \text{and} \quad S_{\delta\gamma} = 2/\lambda_2 \quad \dots\dots\dots\dots (9)$$

As for primary solidification, substituting Eq. (9) into Eq. (8) gives a diffusion length that is equal for all species.

Lengths for diffusion in the γ-solid at the γ/δ and γ/ℓ interfaces can be obtained using Eq. (2) and the boundary

Table 3. Dendrite arm spacings that reproduce measured solidus temperatures.

			Composition							Measured solidus	t_f	λ_2
C	Si	Mn	P	S	Cr	Ni	Mo	Cu	V	(± 15 K)[22]	(s)	(μm)
0.55	0.27	0.50	0.019	0.012	0.99	3.0	0.31	0.06	0.08	1 663	230	16–30
0.69	0.23	0.72	0.022	0.024	0.02	0.02	0.01	0.03	—	1 628	240	<26
1.01	0.25	0.46	0.012	0.009	0.02	0.03	0.02	0.03	—	1 593	270	<27

conditions (note that $\bar{C}^m_{\gamma\delta} \neq \bar{C}^m_{\delta\gamma}$)

$$C^m_\gamma = \bar{C}^m_{\gamma\delta} \text{ at } x = d_\delta/2 \text{ and } C^m_\gamma = \bar{C}^m_{\gamma\ell} \text{ at } x = d_\gamma/2 \quad ....(10)$$

along with the definition of the volume average γ-solid concentration given in Eq. (4). Then, the diffusion lengths in the γ-solid can be shown to be

$$l^m_{\gamma\delta} = \left\{ \frac{12}{(d_\gamma - d_\delta)} - \frac{4}{(d_\gamma - d_\delta)} \frac{(\bar{C}^m_{\gamma\delta} - \bar{C}^m_{\gamma\ell})}{(\bar{C}^m_{\gamma\delta} - \langle C^m_\gamma \rangle^\gamma)} \right\}^{-1} \quad ....(11)$$

$$l^m_{\gamma\ell} = \left\{ \frac{12}{(d_\gamma - d_\delta)} - \frac{4}{(d_\gamma - d_\delta)} \frac{(\bar{C}^m_{\gamma\ell} - \bar{C}^m_{\gamma\delta})}{(\bar{C}^m_{\gamma\ell} - \langle C^m_\gamma \rangle^\gamma)} \right\}^{-1} \quad ....(12)$$

For the geometry in Fig. 1(b), the length d_γ and the interfacial area concentrations $S_{\gamma\ell}$ are

$$d_\gamma = (\varepsilon_\delta + \varepsilon_\gamma)\lambda_2 \text{ and } S_{\gamma\ell} = 2/\lambda_2 \quad ....(13)$$

Note that unlike the diffusion length in the δ-solid, $l^m_{\gamma\delta}$ and $l^m_{\gamma\ell}$ are different for different species.

In contrast with primary solidification, it is not possible to obtain a simple analytical relationship between the liquid composition and the solid factions during peritectic solidification with no macroscopic solute transport, and a numerical time integration scheme must be employed. Given a prescribed cooling rate and using an implicit numerical scheme, for example, the γ/ℓ phase change rate can be determined by substituting the discretized liquid species conservation equation for each element for the liquid concentrations in the expression for the liquidus temperature, and finding the root ($\Gamma_{\gamma\ell}$) of the resulting non-linear equation. Similarly, the γ/δ phase change rate ($\Gamma_{\gamma\delta}$) can be determined by combining the expression for the γ/δ-interface temperature with the γ/δ-interfacial species balance and the discretized solid (both δ- and γ-) species conservation equations. (Using this procedure, it is necessary to iterate on the concentrations and phase change rates within each time step). Comparison of peritectic microsegregation calculations using the diffusion length model described here with previous calculations and experimental measurements will be described in a future study.

2.3. Numerical Procedure

For the simulations discussed in Chap. 3, an implicit, control-volume based finite difference scheme has been used to discretize the conservation equations, and a power law scheme used to evaluate the finite difference coefficients. The velocity-pressure coupling in the momentum equations was handled using the SIMPLER algorithm.[28] The method used to couple the energy and species conservation equations in the mushy zone to calculate the solid fractions is described by Schneider and Beckermann.[9] Computations were performed on a 42×82 grid with a time step of 0.25 s. For a ten element multicomponent simulation, 1 sec of simulation time requires approximately 1 150 sec of cpu time on an HP 715/50 workstation.

3. Results and Discussion

In order to illustrate the use of the model to predict the formation of macrosegregation, the solidification of a ten element austenitic steel alloy, with initial com-

Table 4. Thermophysical properties of steel.

Densities[33]	Thermal expansion[10]
$\rho_\gamma = \rho_\ell = 7\,300 \text{ kg/m}^3$	$\beta_T = 2.0 \times 10^{-4} \text{ K}^{-1}$
Specific heats[34,35]	Thermal conductivities[34,35]
$\partial \langle h_\gamma \rangle^\gamma / \partial T = 650 \text{ J/kg/K}$	$k_\gamma = 30 \text{ W/m/K}$
$\partial \langle h_\ell \rangle^\ell / \partial T = 800 \text{ J/kg/K}$	$k_\ell = 27 \text{ W/m/K}$
Liquid viscosity[33]	Liquid mass diffusivities[33]
$\mu_\ell = 6.0 \times 10^{-4} \text{ kg/m/s}$	$D^m_\ell = 2 \times 10^{-9} \text{ m}^2/\text{s}$
Latent heat[10]	Dendrite arm spacings
$\langle h_\ell \rangle^\ell - \langle h_\gamma \rangle^\gamma = 270 \times 10^3 \text{ J/kg}$	$\lambda_1 = 350 \,\mu\text{m}$
	$\lambda_2 = 25 \,\mu\text{m}$

Permeability- parallel to primary dendrite arms[8]

$$K_{\xi\xi} = \begin{cases} [4.53 \times 10^{-4} + 4.02 \times 10^{-6}(\varepsilon_\ell + 0.1)^{-5}] \dfrac{\lambda_1^2 \varepsilon_\ell^3}{(1 - \varepsilon_\ell)} \\ \qquad\qquad\qquad\qquad\qquad\qquad \text{for } \varepsilon_\ell < 0.7 \\ 0.07425\lambda_1^2[-\ln(1 - \varepsilon_\ell) - 1.487 + 2(1 - \varepsilon_\ell) - 0.5(1 - \varepsilon_\ell)^2] \\ \qquad\qquad\qquad\qquad\qquad\qquad \text{for } \varepsilon_\ell \geq 0.7 \end{cases}$$

Permeability perpendicular to primary dendrite arms[8]

$$K_{\eta\eta} = \begin{cases} \left[1.73 \times 10^{-3} \left(\dfrac{\lambda_1}{\lambda_2} \right)^{1.09} \right] \dfrac{\lambda_2^2 \varepsilon_\ell^3}{(1 - \varepsilon_\ell)^{0.749}} \quad \text{for } \varepsilon_\ell < 0.7 \\ 0.03979\lambda_1^2[-\ln(1 - \varepsilon_\ell) - 1.476 + 2(1 - \varepsilon_\ell) \\ \qquad - 1.774(1 - \varepsilon_\ell)^2 + 4.076(1 - \varepsilon_\ell)^3] \quad \text{for } \varepsilon_\ell \geq 0.7 \end{cases}$$

position as given in Table 2, was simulated. Note that the alloy composition is such that only γ-solid will form, so that there is no peritectic transformation. The domain used for the simulations was a two-dimensional rectangular cavity of 0.2 m height and 0.1 m width, with insulated top, bottom and right walls, that was cooled at the left wall via an overall heat transfer coefficient of 150 W/m²/K and an ambient temperature of 293 K. The initial condition was a quiescent melt at a uniform temperature of 1 813 K and uniform composition. Thermophysical properties for steel (as well as relations for the mushy zone permeability) are summarized in **Tables 2** and **4**. Since the permeabilities decrease with decreasing liquid fraction, the velocities in the mushy zone are naturally dampened during solidification. Note, also, that flow due to solidification shrinkage is not included (*i.e.*, $\rho_\gamma = \rho_\ell$).

The results of the simulation are summarized in **Figs. 3** through **6**. The shaded macrosegregation plots used in the discussion of the results are of the normalized mixture concentration, *i.e.*, $C^m_{\min}/C^m_{\text{in}} = (\varepsilon_\ell \rho_\ell \langle C^m_\ell \rangle^\ell + \varepsilon_\gamma \rho_\gamma \langle C^m_\gamma \rangle^s)/(\varepsilon_\ell \rho_\ell + \varepsilon_\gamma \rho_\gamma)/C^m_{\text{in}}$ with maximum and minimum values given at the top of the figures, and a scale provided.

3.1. Intermediate Stages of Solidification

Figure 3(a) shows that after 750 sec of cooling a portion of the casting next to the cooled wall has completely solidified, and the mushy zone extends across about two-thirds of the casting. The velocity vectors show the flow in the bulk melt is generally counterclockwise. Flow through the mushy zone is mostly downward with some upflow near the casting bottom, where a channel is forming (indicated by the dashed lines).

Due to different solubilities of the elements in the solid and liquid, the formation of solid is accompanied by an enrichment of the interdendritic liquid with solute. The flow through the mushy zone, as well as the bulk melt,

redistributes this enriched liquid, as illustrate for carbon in **Fig. 3(b)**. Pooling of solute rich liquid at the casting bottom is visible, and the solid fraction contours in **Fig. 3(a)** shows that this has delayed the formation of solid in that region. Some of this enriched liquid has also been carried upwards through the channel at the casting bottom and into the bulk liquid. Macrosegregation of the other elements is similar to that of carbon, with the severity of segregation dependent on the partition coefficient of the element (e.g., most severe segregation for sulfur, which has the smallest partition coefficient).

One consequence of the differing extent of segregation of the elements is the formation of small islands of mush along the right wall as shown in Fig. 3(a). The complex dependence of the liquidus temperature on the liquid composition means that even though a region of the melt is highly enriched in some elements, a smaller degree of enrichment of other elements in that region elevates the liquidus temperature and leads to the formation of the islands. While they are porous, the islands offer resistance to the flow which affects the velocity field, as indicated in Fig. 3(a) by the strong flow between the two islands at the casting bottom. In reality, one would expect the islands to be made up of equiaxed crystals that would be free to move (i.e., settle or float) in the melt, something the present model does not account for.

Before leaving Fig. 3, it is interesting to note that the flow through the mushy zone is downwards (i.e., in the direction of thermal buoyancy driven flow) even though the enrichment of the liquid in the mushy zone with solute serves to decrease the density of the liquid (i.e., β_C^m in Table 2 is positive for most of the elements). This is explained by the fact that, for the alloy under consideration, carbon dominates the total buoyancy force in the mushy zone, with the effects of thermal buoyancy outweighing those due to solutal buoyancy.[9]

3.2. Final Macrosegregation Patterns

After 2 250 sec, solidification of the casting is completed. The final macrosegregation patterns for nickel, silicon, carbon and sulfur are shown in **Fig. 4**. Due to the continuous drawing of solute rich liquid downward and out of the mushy zone, the solid near the left and top walls of the casting is solute poor, while the bottom and right is solute rich. Segregated channels are visible, with the compositional differences between the channels and surrounding solid being especially large for sulfur, which has a small partition coefficient. Overall, the macrosegregation patterns for the elements are similar, with the severity of segregation inversely proportional to the partition coefficient of the element (i.e., more severe segregation for smaller partition coefficients).
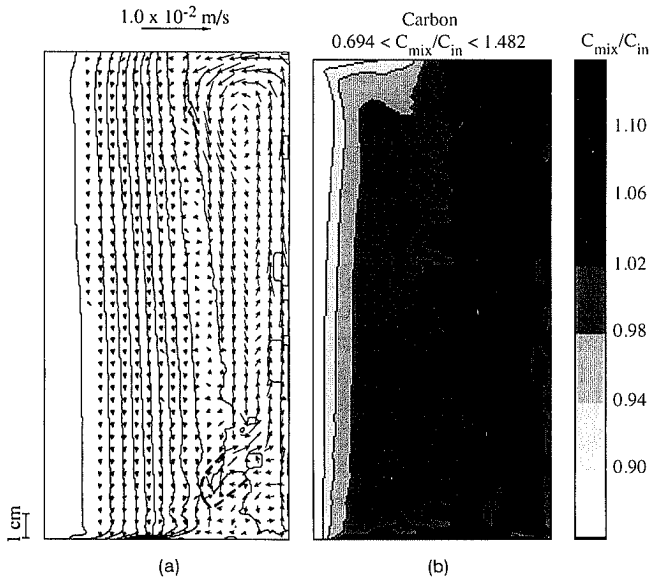
Fig. 3. Simulation results at 750 sec (a) velocity field and solid fraction contours and (b) normalized mixture concentration of carbon.
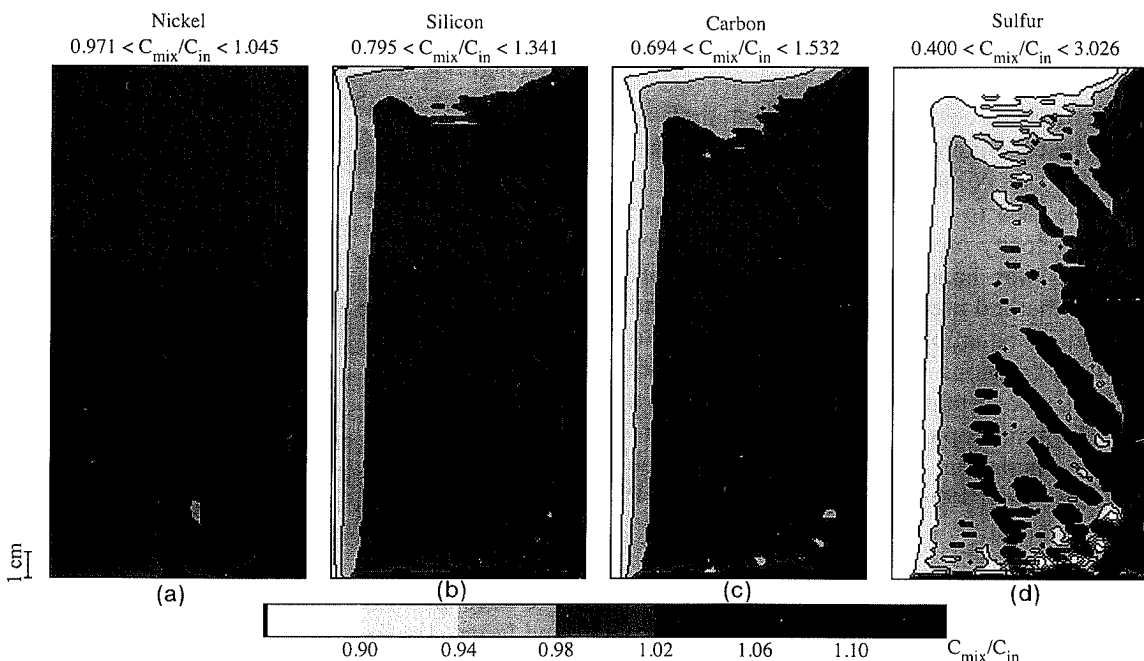
Fig. 4. Final simulated macrosegregation patterns: (a) nickel, (b) silicon, (c) carbon, and (d) sulfur.
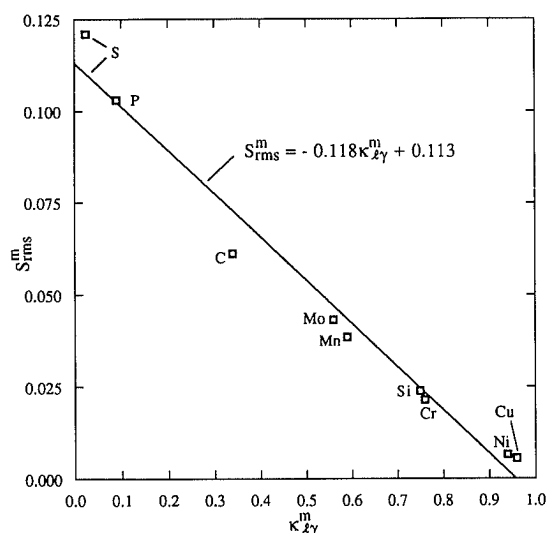
Fig. 5. Global extent of macrosegregation of the elements as a function of partition coefficient.

Fig. 6. Normalized segregation along the horizontal centerline ($y=0.10$ m) of the casting.

3.3. Scaling of Macrosegregation

To further explore the relative segregation of the elements, **Fig. 5** provides a comparison of the global extent of macrosegregation of each of the elements. The plotted values are of

$$S_{\text{rms}}^{m} = \left\{ \frac{1}{V_{\text{casting}}} \iiint\limits_{V_{\text{casting}}} \left[\frac{\langle C_{\gamma}^{m} \rangle^{\gamma}}{C_{\text{in}}^{m}} - 1 \right]^{2} dV \right\}^{1/2} \quad \text{.......} \quad (14)$$

at the end of solidification, which is a measure of the net macrosegregation of an element throughout the casting. The curve fit in Fig. 5 shows that the severity of macrosegregation is approximately linearly dependent on the partition coefficient of the element.

In light of the results in Fig. 5, the remaining question is whether the local element concentrations can also be scaled with their partition coefficients. **Figure 6** indicates that the absolute value of the local segregation of sulfur, normalized by S_{rms}^{S}, along the horizontal centerline of the casting is different by up to a factor of 2 from that of manganese and carbon, especially along the right half of the centerline. This is most likely due to the fact that the partition coefficient of sulfur is very small (an order of magnitude smaller than that for carbon and manganese). The discrepancy between the profiles in **Fig. 6** indicates that although the global extent of segregation of an element can be scaled with its partition coefficient, local scaling of the concentrations is not possible for elements with widely varying partition coefficients.

4. Conclusions

A method for incorporating finite-rate solid solute diffusion and a microscopic model of the peritectic transformation into a macroscopic model for the solidification of multicomponent steel alloys has been described. By considering finite-rate solid microsegregation, the solidus temperatures of multicomponent austenitic steels were shown to be accurately calculated. Comparison of microsegregation calculations for peritec-

tic solidification with previous calculations and measurements will be reported in the near future. A representative simulation of the solidification of a ten element austenitic steel in a rectangular cavity cooled from the side showed the formation of macrosegregation, channel segregates, and "islands" of mush surrounded by the bulk melt. The global extent of macrosegregation of an element was found to be linearly dependent on its partition coefficient, but local scaling of the concentrations was not possible for large differences in the partition coefficients of the elements. Macroscopic simulations of the peritectic solidification of multicomponent steels will also be reported in the near future. Other work planned in the development of the model includes the incorporation of more precise thermodynamic equilibrium calculations and comparison of model predictions with experiments.
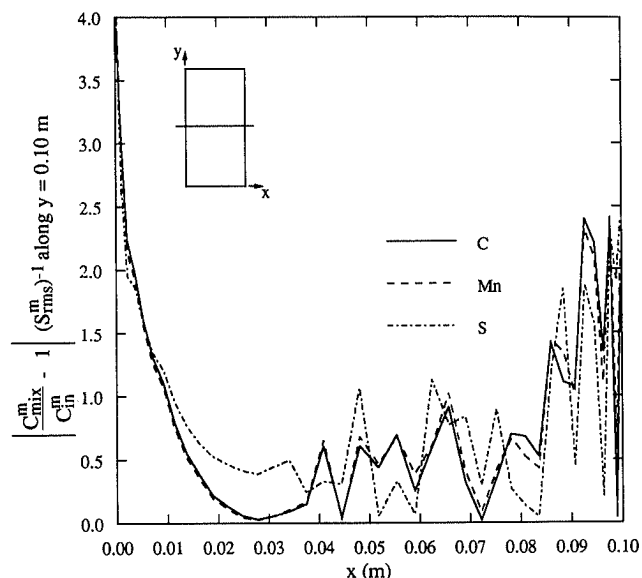
Nomenclature

C: concentration (wt%)

d: mean characteristic length of solid phase (m)

D: mass diffusivity (m^2/s)

g: acceleration of gravity (m/s^2)

h: enthalpy (J/kg)

k: thermal conductivity (W/m/K)

$K^{(2)}$: second-order permeability tensor (m^2)

l: diffusion length scale (m)

m_{kj}: change in j/k interfacial temperature with concentration (K/wt%)

p: pressure (N/m^2)

S: interfacial area concentration (m^{-1})

S_{rms}: rms value of net macrosegregation

t: time (s)
t_f: local solidification time (s)
T: temperature (K)
T_f: pure iron melting temperature (K)
T_p: peritectic temperature (K)
v: velocity vector (m/s)
V: volume (m^3)

Greek Symbols

α: diffusion Fourier number
β_C: solutal expansion coefficient ((wt%)$^{-1}$)
β_T: thermal expansion coefficient (K^{-1})
ε_k: volume fraction of phase k
Γ: phase change rate (kg/m^3/s)
κ: partition coefficient (wt%/wt%)
λ: dendrite arm spacing (m)
μ: kinematic viscosity (kg/m/s)
ρ: density (kg/m^3)
Ψ_k: a quantity of a phase k

Subscripts

in: initial
j: phase j
k: phase k
kj: k/j interface
ℓ: liquid
mix: mixture
s: solid
δ: ferrite
γ: austenite
1: primary
2: secondary

Superscripts

C: carbon
m: species m
t: transpose of a tensor
—: interfacial average

REFERENCES

1) W. D. Bennon and F. P. Incropera: *Metall. Trans. B.*, **18B** (1987), 611.
2) C. Beckermann and R. Viskanta: *Physico Chem. Hydrodyn.*, **10** (1988), 195.
3) V. R. Voller, A. D. Brent and C. Prakash: *Int. J. Heat Mass Transfer*, **32** (1989), 1719.
4) G. Amberg: *Int. J. Heat Mass Transfer*, **34** (1991), 217.
5) S. D. Felicelli, F. C. Heinrich and D. R. Poirier: *Metall. Trans. B*, **22** (1991), 847.
6) P. J. Prescott and F. P. Incropera: *Metall. Trans. B*, **22B** (1991), 529.
7) Q. Z. Diao and H. L. Tsai: *Metall. Trans. A*, **24A** (1993), 963.
8) M. C. Schneider and C. Beckermann: Transport Phenomena in Solidification, ASME HTD–Vol. 284, (1994), 43.
9) M. C. Schneider and C. Beckermann: *Metall. and Mat. Trans. A*, (1995), in press.
10) T. Fujii, D. R. Poirier and M. C. Flemings: *Metall. Trans. B.*, **10B** (1979), 331.
11) D. R. Poirier and M. M. Andrews: Proc. of 1st Int. Steel Foundry Congress, Steel Foundrymens' Society of America, Des Plaines, Illinois, (1985), 307.
12) F. Roch, H. Combeau, I. Poitrault, J. Ch. Chevrier and G. Lesoult: Proc. of 6th Int. Iron and Steel Cong., ISIJ, Tokyo, (1990), 665.
13) H. Combeau, F. Roch, I. Poitrault, J. Ch. Chevrier and G. Lesoult: Adv. Comp. Methods in Heat Transfer, Vol. 3: Phase Change and Combustion Simultaion, Springer-Verlag, New York, (1990), 79.
14) F. Roch, H. Combeau, J. Ch. Chevrier and G. Lesoult: Modell. of Casting, Welding and Adv. Solid. Proc. V, TMS, Warrendale, Pennsylvania, (1991), 789.
15) H. Vannier, H. Combeau and G. Lesoult: Num. Methods in Ind. Forming Proc., A. A. Balkema, Rotterdam, (1992), 835.
16) M. C. Schneider: Modeling the Columnar Dendritic Solidification of Lead-Tin Alloys, M. S. Thesis, The University of Iowa, Iowa City, Iowa, (1991).
17) C. Beckermann and R. Viskanta: *Appl. Mechanics Rev.*, **46** (1993), 1.
18) J. Ni and C. Beckermann: *Metall. Trans. B*, **22B** (1991), 349.
19) C. Y. Wang and C. Beckermann: *Metall. Trans. A*, **24A** (1993), 2787.
20) Y. Ueshima, S. Mizoguchi, T. Matsumiya and H. Kajioka: *Metall. Trans. B.*, **17B** (1986), 845.
21) P. J. Bunyan, S. Dellar and N. Blake: *Mater. Forum*, **16** (1992), 215.
22) J. Miettinen: *Metall. Trans. A*, **23A** (1992), 1155.
23) K. Matsuura, Y. Itoh and T. Narita: *ISIJ Int.*, **33** (1993), 583.
24) I. Ohnaka: *Trans. Iron Steel Inst. Jpn.*, **26** (1986), 1045.
25) C. Y. Wang and C. Beckermann: *Mater. Sci. Eng.*, **A171** (1993), 199.
26) M. Rappaz and V. R. Voller: *Metall. Trans. A*, **21A** (1990), 749.
27) D. R. Poirier, P. J. Nandapurkar and S. Ganesan: *Metall. Trans. B*, **22B** (1991), 889.
28) S. V. Patankar: Numerical Heat Transfer and Fluid Flow, McGraw-Hill, New York, (1980).
29) M. C. Schneider and C. Beckermann: Tech. Rep. UIME-CB01-1993, Dept. of Mech. Eng., The Univ. of Iowa, Iowa City, Iowa, (1993).
30) J. Wanqi and S. Yaohe: *Metall. Trans. B*, **20B** (1989), 723.
31) M. A. Krishtal: Diffusion Processes in Iron Alloys, trans. from Russian by Israel Program for Scientific Translations, Jerusalem, (1970).
32) A. Kagawa and T. Okamoto: *Mater. Sci. Technol.*, **2** (1986), 997.
33) Landolt and Börnstein: Zahlenwerte der Physik und Chemie, Teil 5, Bandteil a, Springer-Verlag, Berlin, (1969).
34) R. D. Pehlke, A. Jeyarajan and H. Wada: National Technical Information Service, Document No. PB 83-211003, Ann Arbor, Michigan, (1982).
35) Y. S. Touloukain, R. W. Powell, C. Y. Ho and P. B. Klemens: Thermophysical Properties of Matter, Vol. 1, IFI/Plenum, New York, (1970).